Editors' Suggestion

Spin-orbit splitting of Ar^+, Kr^+, and Kr^{2+} determined by strong-field ultrahigh-resolution Fourier-transform spectroscopy

Toshiaki Ando, Alex Liu,* Naoki Negishi,† Atsushi Iwasaki, and Kaoru Yamanouchi‡
Department of Chemistry, School of Science, The University of Tokyo, 7-3-1 Hongo, Bunkyo-ku, Tokyo 113-0033, Japan

(Received 14 June 2021; accepted 26 August 2021; published 15 September 2021)

By the Fourier transform of the yields of Ar^{2+} and Kr^{2+} obtained by the pump-probe measurements using intense near-infrared few-cycle laser pulses, we determined the spin-orbit splitting energies in the electronic ground states of Ar^+, Kr^+, and Kr^{2+} with high precision. For Ar^+ and $^{84}Kr^+$, the spin-orbit splitting energies for $^2P_{1/2} - {}^2P_{3/2}$ were determined to be 1431.583 33(12) and 5370.296 42(50) cm^{-1} and the isotope effect was examined for $^{83}Kr^+$, $^{84}Kr^+$, and $^{86}Kr^+$. For $^{84}Kr^{2+}$, the spin-orbit splitting energies for $^3P_1 - {}^3P_2$ and $^3P_0 - {}^3P_2$ were determined to be 4548.2144(40) and 5312.8059(40) cm^{-1}, respectively.

DOI: 10.1103/PhysRevA.104.033516

I. INTRODUCTION

Determination of the splitting energy between the spin-orbit sublevels of the electronic ground states of rare-gas atom cations with high precision has been a challenging problem in high-resolution spectroscopy. Because the optical transitions between the spin-orbit sublevels are forbidden, the splitting energies of Ne^+ [1], Ar^+ [2], Kr^+ [3], and Xe^+ [4] were determined by the measurements of the emission transitions from the electronically highly excited states to the spin-orbit sublevels. The resolutions achieved by the spectroscopic measurements were on the order of 0.1 cm^{-1}.

In 1985, Yamada *et al.* recorded the $^2P_{1/2} - {}^2P_{3/2}$ transitions of Ne^+ and Ar^+ in the IR wavelength region by Zeeman modulation spectroscopy [5], and determined the spin-orbit splitting energies of Ne^+ and Ar^+ to be 780.4240(11) cm^{-1} and 1431.5831(7) cm^{-1}, respectively. In the 2000s, by high-resolution photoionization spectroscopy, the energy levels of the high-lying Rydberg states of the neutral isotope species of Kr and Xe were determined with uncertainty as small as 10^{-2} cm^{-1} [6–12] and the fine-structure splitting energies and the hyperfine-structure energies of Kr^+ [9–12] and Xe^+ [7,8] were determined by Merkt and his co-workers by the analysis based on multichannel quantum defect theory.

On the other hand, recent advances in ultrashort-pulsed laser technology enabled us to create an electronic wave packet composed of the spin-orbit sublevels of rare-gas atom cations by strong-field ionization [13–19]. Goulielmakis *et al.* observed the coherent oscillatory motion of an electron wave packet created by the strong-field ionization of Kr^+ by attosecond transient absorption spectroscopy [15]. Because such oscillation appearing in the time domain carries the information of the spin-orbit levels, the Fourier transform of the oscillation will give us spectroscopic information with high precision if the oscillation is recorded for a sufficiently long period of time.

As has been demonstrated for CH_3OH and CH_3OH^+ [20,21] and D_2 and D_2^+ [22], spectroscopic information of atoms and molecules in the frequency domain can also be extracted with high resolution by the pump-probe measurements in the time domain in which ultrashort intense laser pulses are employed. In 2018, we determined the rovibrational level structure of D_2^+ with uncertainty as small as 0.0002 cm^{-1} by strong-field ultrahigh-resolution Fourier transform (SURF) spectroscopy [22], in which the yields of D_2^+ and D^+ created by the irradiation of the ultrashort pump laser pulse were probed by the ultrashort probe laser pulse.

In the present study, by SURF spectroscopy using intense few-cycle near-IR pump and probe laser pulses, we determine the energy separation between the lowest spin-orbit sublevels of $^2P_{1/2}$ and $^2P_{3/2}$ of Ar^+ and that of the Kr^+ with uncertainties of 1.2×10^{-4} and 5×10^{-4} cm^{-1}, respectively, and the energy separation of the lowest spin-orbit sublevels between $^3P_0$ and $^3P_2$ and that between $^3P_1$ and $^3P_2$ of Kr^{2+} with an uncertainty of 0.004 cm^{-1}. These uncertainties are significantly smaller than those reported before by high-resolution Zeeman modulation spectroscopy (for Ar^+) and high-resolution photoionization spectroscopy (for Kr^+ and Kr^{2+}).

II. EXPERIMENT

The details of the experimental setup can be found in Ref. [22]. We introduce linearly polarized near-infrared few-cycle intense laser pulses (5 fs, 780 nm) into a Michelson interferometer to produce pump and probe laser pulses and record the time delay created by the interferometer using a frequency-stabilized He-Ne laser (HRS015B, Thorlabs, Inc.). We focus these pulses with the focal intensity of 4.5×10^{14} W/cm^2 onto an effusive molecular beam of a mixture of

*Present address: Department of Chemistry, Massachusetts Institute of Technology, 77 Massachusetts Avenue, Cambridge, MA 02368, USA.
†Present address: Department of Arts and Sciences, Graduate School of Arts and Sciences, The University of Tokyo, Komaba, Meguro-ku, Tokyo 153–8902, Japan.
‡kaoru@chem.s.u-tokyo.ac.jp

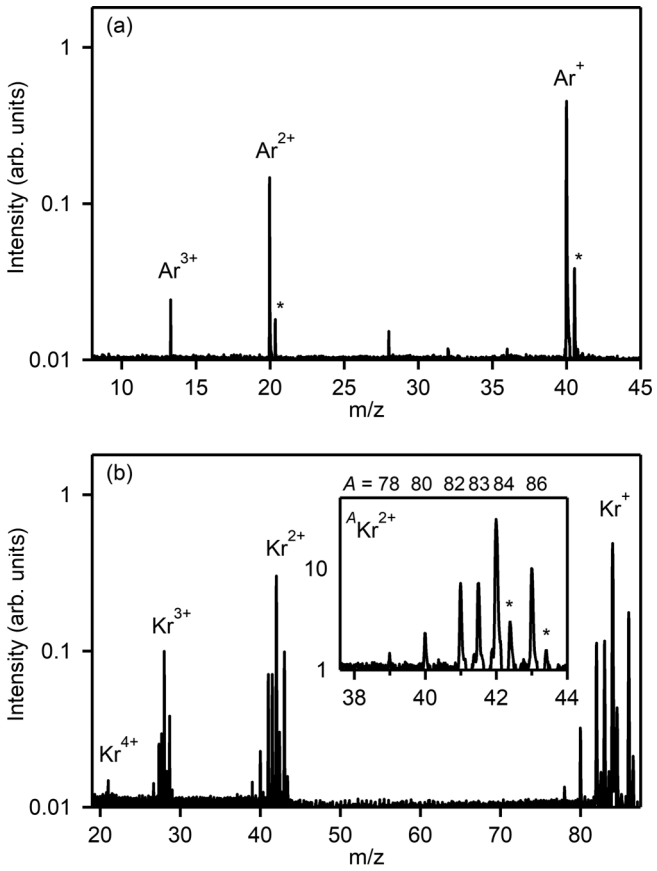

FIG. 1. TOF spectra of Ar (a) and Kr (b) on a logarithmic scale. The inset in (b) shows the expanded TOF spectrum of Kr^{2+}. The peaks with an asterisk in (a) are ringing signals of Ar^+ and Ar^{2+} and those in (a) are ringing signals of $^{84}Kr^{2+}$ and $^{86}Kr^{2+}$ in (b), originating from the impedance mismatch in the electric circuit in the detection system.

Ar and D_2 with the partial pressure ratio of $p(\mathrm{Ar}) : p(\mathrm{D_2}) = 3 : 7$ for the measurements of Ar^+ and that of a mixture of Kr and D_2 [$p(\mathrm{Kr}) : p(\mathrm{D_2}) = 1 : 1$] for the measurements of Kr^+ and Kr^{2+} in a time-of-flight (TOF) mass spectrometer. We record the yields of doubly charged atomic ions, that is, Ar^{2+} for the measurements of Ar^+ and $^{83}Kr^{2+}$, $^{84}Kr^{2+}$, and $^{86}Kr^{2+}$ for the measurements of Kr^+, to determine the energy separations between a pair of the spin-orbit sublevels. Simultaneously, we record the yield of $D_2{}^+$ as a function of the pump-probe time delay for the frequency calibration of the Fourier transform spectrum of the rare-gas atom cations.

III. RESULTS AND DISCUSSION

A. Ar^+ and Kr^+

1. TOF spectra and time-dependent ion yields

Figures 1(a) and 1(b) show, respectively, the TOF spectra obtained when sample gases of Ar and Kr are irradiated with few-cycle laser pulses. The highly charged cations up to $n = 3$ can be seen for Ar^{n+} and those up to $n = 4$ can be seen for Kr^{n+}. In the inset of Fig. 1, the TOF spectrum for the isotopes $^{A}Kr^{2+}$ ($A = 78$, 80, 82, 83, 84, and 86) is shown. The peak intensities of the isotopes reflect the natural abundance of Kr, 0.35, 2.25, 11.6, 11.5, 57.0, and 17.3% for $A = 78$, 80, 82, 83, 84, and 86, respectively [23].

As shown in Fig. 2(a), the yields of Ar^{2+} and $^{84}Kr^{2+}$ vary as a function of the pump-probe delay. The oscillation in the yield of Ar^{2+} exhibits the period of ∼23.3 fs, corresponding to the energy separation of the two spin-orbit levels of $^2P_{1/2}$ and $^2P_{3/2}$ of Ar^+. The oscillation in the yield of $D_2{}^+$ exhibits the period of ∼11.2 fs, which corresponds to the fundamental vibrational frequency of neutral D_2 [24].

The Fourier transform spectra of the ion yields of Ar^{2+}, $^{84}Kr^{2+}$, and $D_2{}^+$ in the pump-probe time-delay range of $\sim 1\,\mathrm{ps} < \Delta t <\sim 500\,\mathrm{ps}$ are shown in Figs. 2(b)–2(d), respectively. A sharp peak appearing at $\sim 1430\,\mathrm{cm^{-1}}$ shown in Fig. 2(b) corresponds to the spin-orbit splitting energy of Ar^+. In the Fourier transform spectrum of $^{84}Kr^+$ shown in Fig. 2(c), a sharp peak appears at $\sim 5370\,\mathrm{cm^{-1}}$ corresponding to the spin-orbit splitting of $^{84}Kr^+$, even though the corresponding oscillation in the time domain is not clearly identified in Fig. 2(a). In Fig. 2(d), the rotational energy separations assigned to D_2 and $D_2{}^+$ appear in the low-frequency region ($<700\,\mathrm{cm^{-1}}$) and the fundamental vibrational energy separations of $D_2{}^+$ can be seen in the range of 1000–1600 $\mathrm{cm^{-1}}$ [22]. In the inset of Fig. 2(d), a well-resolved rotational structure can be seen at the fundamental vibrational energy separation of neutral D_2.

2. The origin of the yield oscillations

A strong-field ionization of rare-gas atoms induced by the irradiation of few-cycle laser pulses creates an electron hole in the outermost valence p orbital as schematically shown in Fig. 3. Because an electron in the $m_L = 0$ orbital is preferentially ejected upon the ionization induced by a pump laser pulse, an electron hole is created in the $m_L = 0$ orbital just after the ionization. According to the Ammosov-Delone-Krainov (ADK) theory [25,26], the probability of the ionization from the $m_L = 0$ orbital of Ar and Kr is 11 times and 9.2 times as large as that of the ionization from $m_L = \pm 1$, respectively. Because of the existence of the spin-orbit interaction, the created electronic state, ^2P ($m_L = 0$), is not a stationary state and expressed as a coherent superposition of the two spin-orbit sublevels, that is, the $^2P_{1/2}$ and $^2P_{3/2}$ states. Therefore, the populations in the ^2P ($m_L = 0$) state as well as that in the ^2P ($m_L = 1$) state oscillate with the period corresponding to the energy separation E_{SO} between the $^2P_{1/2}$ and $^2P_{3/2}$ state. The oscillation of the populations in the ^2P ($m_L = 0$) and ^2P ($m_L = 1$) states appears as the oscillation of the yield of doubly charged rare-gas atoms produced by the irradiation of the probe laser pulse. This is because the ionization probabilities of the ^2P ($m_L = \pm 1$) states to the doubly charged ions, $\Gamma_{\pm 1}$, are larger than those of the ^2P ($m_L = 0$) states, Γ_0. The ratio $\Gamma_{\pm 1}/\Gamma_0$ for Ar^+ and that for Kr^+ are calculated to be 8.2 and 6.8, respectively, when the light-field intensity is $4.5 \times 10^{14}\,\mathrm{W/cm^2}$ as explained below.

The motion of the electron wave packet in a rare-gas atom cation produced after photoionization can be characterized in terms of the reduced density matrix [27]. The wave function of a rare-gas atom ionized to the ^2P states and a photoelectron

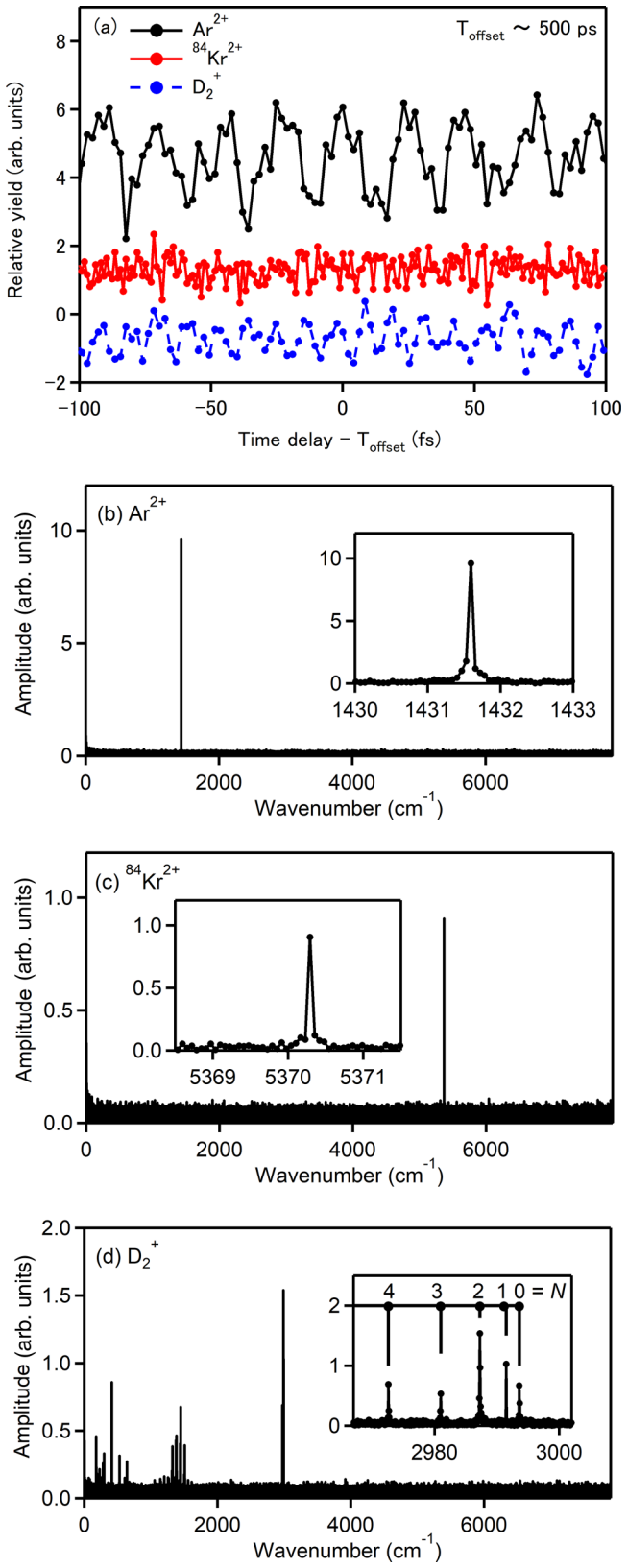

FIG. 2. (a) The time-delay dependent ion yield of Ar^{2+} (black curve) and $^{84}Kr^{2+}$ (red curve) at $\Delta t \sim 500$ ps. The ion yield of D_2^+ (blue broken line) was used for the fine calibration of the Fourier transform spectra. Fourier transform spectra of the ion yields are shown for (b) Ar^{2+}, (c) $^{84}Kr^{2+}$, and (d) D_2^+. An inset in each spectrum shows an expanded view of the peak profiles.

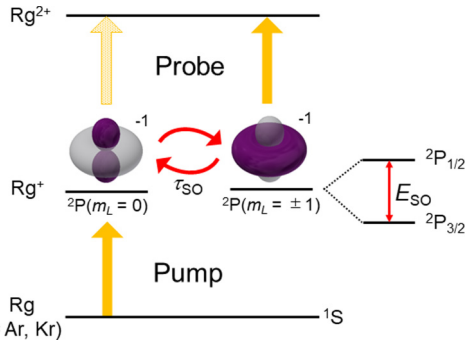

FIG. 3. Energy diagram of a rare-gas atom and its cation. The pump pulse creates ^2P ($m_L = 0$) state through a strong-field ionization of neutral atoms and the population of the ^2P ($m_L = 0$) state oscillates by the spin-orbit interaction with the period corresponding to the spin-orbit energy separation of E_{SO}.

can be expressed using the expansion coefficients, $a_{J m_J k}$, as

$$|\Psi(t)\rangle = \sum_{J m_J k} a_{J m_J k} \exp\left(-\frac{i(E_J + E_k)t}{\hbar}\right)|J, m_J\rangle|\phi_k\rangle, \quad (1)$$

where $|J, m_J\rangle$ is the wave function of an electronic eigenstate of the resultant rare-gas atom cation, E_J is the eigenenergy for the rare-gas atom cation, $|\phi_k\rangle$ is the eigenstate of the photoelectron, and E_k is the eigenenergy for the photoelectron. The reduced density matrix elements of the rare-gas atom cation, $\rho_{J,J'}^{m_J,m_{J'}}(t)$, are written as

$$\begin{aligned}\rho_{J,J'}^{m_J,m'_J}(t) &= \sum_k \langle J, m_J|\phi_k|\Psi(t)\rangle\langle\Psi(t)|\phi_k\rangle|J', m'_J\rangle \\ &= \exp\left(\frac{i(E_{J'} - E_J)t}{\hbar}\right)\sum_k a^*_{J m_J k} a_{J' m'_J k} \\ &= \exp\left(\frac{i(E_{J'} - E_J)t}{\hbar}\right)\rho_{J,J'}^{m_J,m'_J}. \end{aligned} \quad (2)$$

Because the ionization rate of the rare-gas atom cation can be expressed as a sum of the ionization rate from all the valence orbitals as proposed in Ref [28], the ionization probability depends on the electron configuration. When we denote the ionization rate from the $|L, m_L, S, m_S\rangle$ state as Γ^+_{L,m_L,S,m_S}, the operator for the ionization rate can be expressed as

$$\hat{\Gamma}^+ = \sum_{m_L,m_S} |L, m_L, S, m_S\rangle\Gamma^+_{L,m_L,S,m_S}\langle L, m_L, S, m_S|, \quad (3)$$

and the time-dependent rate of the ionization of the cation to its dication by the pump pulse is given by

$$\Gamma^+(t) = \sum_{J,J',m_J,m'_J} \langle J, m_J|\hat{\Gamma}^+|J', m'_J\rangle\rho_{J,J'}^{m_J,m'_J}(t). \quad (4)$$

Under the electric dipole approximation, the linearly polarized pump pulse introduces the coherence between the states having the same m_L value, and therefore, only the matrix elements, $\rho_{3/2,\,3/2}^{\pm3/2,\pm3/2}$, $\rho_{3/2,\,3/2}^{\pm1/2,\pm1/2}$, $\rho_{1/2,1/2}^{\pm1/2,\pm1/2}$, $\rho_{3/2,1/2}^{\pm1/2,\pm1/2}$, and $\rho_{1/2,3/2}^{\pm1/2,\pm1/2}$ can take nonzero values. Therefore, the

time-dependent ionization rate can be rewritten simply as

$$\Gamma^+(t) = \sum_{J,m_J} \langle J, m_J|\hat{\Gamma}^+|J, m_J\rangle \rho_{J,J}^{m_J,m_J} + \frac{4\sqrt{2}}{3}(\Gamma^+_{1,1,1/2,1/2} - \Gamma^+_{1,0,1/2,1/2}) \times \mathrm{Re}\left(\rho^{1/2,1/2}_{3/2,1/2}\exp\left(\frac{i(E_{1/2}-E_{3/2})t}{\hbar}\right)\right). \quad (5)$$

Therefore, the ion yield of the dication oscillates with the period of $\frac{h}{E_{1/2}-E_{3/2}} = \frac{h}{E_{\mathrm{SO}}}$ when the pump-probe time delay is scanned, and the amplitude of the oscillation is governed by the difference between the ionization rate $\Gamma^+_{1,1,1/2,1/2}$ and the ionization rate $\Gamma^+_{1,0,1/2,1/2}$.

The ionization rate of the $|L, m_L, S, m_S\rangle$ state is represented as

$$\Gamma^+_{L,m_L,S,m_S} = \sum_{i,j} \left(c_{ij}^{L,M}\right)^2 \Gamma^j_{l_i,m_i}, \quad (6)$$

where $c_{ij}^{L,M}$ is the expansion coefficient representing the projection of the doubly charged rare-gas atom created by the ejection of the ith electron in a valence p orbital specified by a set of quantum numbers $\{l_i, m_i, s_i, m_{Si}\}$ to the electronic state j,

$$c_{ij}^{L,M} = \langle L'_j, M'_j|l_i, -m_i, L, M\rangle\langle S'_j, Ms'_j|s_i, -m_{Si}, S, Ms\rangle, \quad (7)$$

and $\Gamma^j_{l_i,m_i}$ is the ADK ionization rate for the ejection of the ith electron to the electronic state j. When the laser intensity is $4.5 \times 10^{14}\,\mathrm{W/cm^2}$, the ionization enhancement factor defined as $\Gamma^+_{1,1,1/2,1/2}/\Gamma^+_{1,0,1/2,1/2}$ for Ar^+ is calculated to be $\Gamma^+_{1,1,1/2,1/2}/\Gamma^+_{1,0,1/2,1/2} \sim 8.2$ and the ionization enhancement factor for Kr^+ is calculated to be $\Gamma^+_{1,1,1/2,1/2}/\Gamma^+_{1,0,1/2,1/2} \sim 6.8$.

As for ^{83}Kr, the ion yields of $^{83}Kr^{2+}$ reflects the hyperfine splitting because of the existence of the nuclear spin. The oscillation of the ion yield is explained in a similar manner as in the case of ^{84}Kr as will be discussed in Sec. V.

3. Determination of the spin-orbit splitting

The peaks appearing in the inset of Fig. 2(d) representing the energy separation among the rotational levels in the vibrational ground state of D_2 ($N = 0, 1, 2$) were used for the calibration of the Fourier transform (FT) spectra as discussed in Ref. [22]. These peaks were fitted with a function expressed as

$$F(\omega) = Ae^{i\theta}\left[\exp\left(-\left(\frac{t_0}{\alpha}\right)^2\right)\mathrm{erfcw}\left(\pi\alpha\frac{\omega-\omega_0}{\Delta\omega} + \frac{t_0}{\alpha}i\right) - \exp\left(-\left(\frac{t_0-1}{\alpha}\right)^2 - 2\pi i\frac{\omega-\omega_0}{\Delta\omega}\right) \times \mathrm{erfcw}\left(\pi\alpha\frac{\omega-\omega_0}{\Delta\omega} - \frac{t_0-1}{\alpha}i\right)\right], \quad (8)$$

where

$$\mathrm{erfcw(z)} = \frac{2}{\sqrt{\pi}}e^{-z^2}\int_{iz}^{\infty} e^{-x^2}dx \quad (9)$$

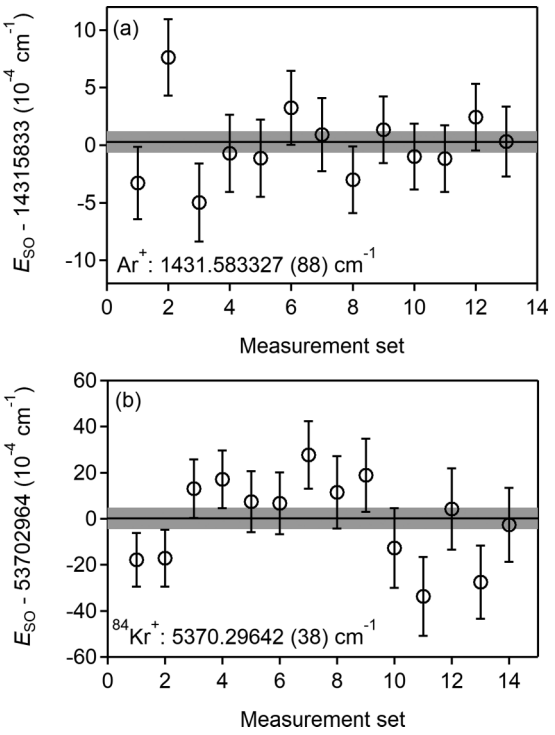

FIG. 4. The spin-orbit splitting energy, E_{SO}, of (a) Ar^+ and (b) $^{84}Kr^+$. The gray area indicates the 1σ uncertainty of the averaged value.

is a scaled complex complementary error function, ω is the frequency of the Fourier transform spectrum, ω_0 is the center frequency of the peak, $\Delta\omega$ is the resolution of the spectrum, t_0 is the center of the Gaussian function in the time domain, α is the width of the Gaussian function in the time domain, A corresponds to the amplitude of the peak, and θ is the phase of the peak (see Appendix A). The frequencies of these three peaks determined from the least-squares fit were used for the fine calibration of the wave number of the Fourier transform spectra using the literature values [29].

The peak appearing in Fig. 2(b) for Ar^{2+} and the peak appearing in Fig. 2(c) for $^{84}Kr^{2+}$ were also fitted with the function $F(\omega)$ and the spin-orbit splitting energies of $E_{\mathrm{SO}}(Ar^+)$ and $E_{\mathrm{SO}}(^{84}Kr^+)$ were determined.

These measurements were performed 13 times for Ar^+ and 14 times for $^{84}Kr^+$ and the results are plotted as shown in Fig. 4. The spin-orbit splitting energies were determined to be $E_{\mathrm{SO}}(Ar^+) = 1431.583\,327\,\mathrm{cm^{-1}}$ with the statistical uncertainty of $8.8 \times 10^{-5}\,\mathrm{cm^{-1}}$ and $E_{\mathrm{SO}}(^{84}Kr^+) = 5370.296\,42\,\mathrm{cm^{-1}}$ with the statistical uncertainty of $3.8 \times 10^{-4}\,\mathrm{cm^{-1}}$. The origins of the systematic uncertainties associated with these spin-orbit splitting values are examined in the next subsection.

4. Estimation of the uncertainties

The origins of the systematic uncertainty associated with the determined spin-orbit splitting energies are considered to be originated from (i) the calibration of the Fourier transform spectra, (ii) the first-order Doppler shift, (iii) the AC Stark

TABLE I. Summary of the source of the uncertainty on the spin-orbit splitting of Ar^+, Kr^+, and Kr^{2+} (10^{-4} cm^{-1}).

	Ar^+	$^{84}Kr^+$	$^{86}Kr^+$	$^{84}Kr^{2+}$	
Level	$^2P_{1/2}-{}^2P_{3/2}$	$^2P_{1/2}-{}^2P_{3/2}$	$^2P_{1/2}-{}^2P_{3/2}$	$^3P_1-{}^3P_2$	$^3P_0-{}^3P_2$
Statistical uncertainty, σ_{stat}	±0.88	±3.8	±5.7	±40	±40
Calibration, σ_{calib}	±0.72	±2.7	±5.0	±4.2	±4.9
First-order Doppler shift, σ_{dop}	±0.41	±1.8	±0.006	0	0
AC Stark shift, σ_{AC}	<0.06	<0.3	<0.3	<0.3	<0.4
Zeeman shift	0	0	0	0	0
Total,[a] σ_{total}	±1.2	±5.0	±7.6	±40	±40

[a]Square root of the sum of the square of the statistical uncertainty and the systematic uncertainties except for σ_{AC}, that is, $\sigma_{total} = \sqrt{\sigma_{stat}^2+\sigma_{calib}^2+\sigma_{dop}^2}$.

shift, and (iv) the Zeeman shift. Their respective contributions are described below and are summarized in Table I.

(i) Calibration: The relative uncertainty ($\Delta E/E$) of the literature values of the fundamental vibrations of D_2 is 5.0×10^{-8}, from which the calibration uncertainty in the spin-orbit spitting value given by $E_{so}\times\Delta E/E$ can be calculated. The calibration uncertainties are 7.2×10^{-5} cm^{-1} for Ar^+ and 2.7×10^{-4} cm^{-1} for $^{84}Kr^+$.

(ii) The first-order Doppler shift: The first-order Doppler shift can be expressed as

$$\frac{\Delta E}{E}=\frac{\bar{v}_{Calib}-\bar{v}_{Rg}}{c}\sin\theta, \tag{10}$$

where $\bar{v}_{Calib}$, $\bar{v}_{Rg}$, c, and θ represent, respectively, the mean velocity of the calibration gas of D_2, the mean velocity of the rare-gas atoms, the speed of light, and the misalignment angle between the laser beam and sample beam (<0.01). At room temperature (300 K), the first-order Doppler shift is estimated to be $<4.1\times10^{-5}$ cm^{-1} for Ar^+ and $<1.8\times10^{-4}$ cm^{-1} for $^{84}Kr^+$.

(iii) AC Stark shift: The AC Stark shift can be written as

$$\Delta E_{Stark}=-\frac{1}{2}\Delta\alpha_{Rg^+}\overline{F_{elec}{}^2}-\frac{f_{Rg^+}}{2f_{D_2}}\Delta\alpha_{D_2}\overline{F_{elec}{}^2}, \tag{11}$$

where F_{elec} represents the residual electric-field amplitude and $\Delta\alpha$ represents the difference between the polarizability in the upper level and the polarizability in the lower level. The first term in the right-hand side represents the AC Stark shift of a rare-gas atom cation and the second term represents the effect of the AC stark shift of D_2. The residual laser-field amplitude can be estimated to be at most $\sim3\times10^{-5}$ a.u., corresponding to the picosecond pulse contrast of $\sim1\times10^{-7}$, and the AC Stark shift on the FT spectrum is at most $\sim6\times10^{-6}$ cm^{-1} for Ar^+ and $\sim3\times10^{-5}$ cm^{-1} for $^{84}Kr^+$.

(iv) Zeeman shift: In the present measurement, the geomagnetism was not shielded, and the Zeeman shift induced by the geomagnetism can be estimated to be $\sim\pm1.4\times10^{-5}$ cm^{-1} for $^2P_{3/2}(M_J=\pm1/2)$. This effect is much smaller than the resolution of the spectrum, and the center of gravity of the Zeeman components is not changed by the Zeeman effect under the first-order approximation. (See Appendix B.)

5. *Isotope effects on* Kr^+

The isotope effect of Kr^+ was examined as shown in Fig. 5. In the case of $^{86}Kr^+$, the peak position seems to be the same as that of $^{84}Kr^+$ as shown in Fig. 5(a) and the peak amplitudes reflect their natural abundances. The FT spectrum of $^{86}Kr^{2+}$ was calibrated by using the peak corresponding to the spin-orbit splitting energy of $^{84}Kr^+$ in the FT spectrum of $^{84}Kr^{2+}$ and the spin-orbit splitting energy of $^{86}Kr^+$ is obtained by the fitting to be $E_{SO}(^{86}Kr^+)=5370.295\,73(76)$ cm^{-1}. The sources of the uncertainty are summarized in Table I. Because the spin-orbit energy of $^{84}Kr^+$ is used for the calibration, the first-order Doppler shift is only 6×10^{-7} cm^{-1}, and the uncertainty of the spin-orbit splitting energy of $^{84}Kr^+$ is the uncertainty of the calibration. The difference between the spin-orbit splitting energy for $^{86}Kr^+$ and that for $^{84}Kr^+$, $E_{SO}(^{86}Kr^+)-E_{SO}(^{84}Kr^+)$, is obtained to be $-0.00069(57)$ cm^{-1} and only the statistical uncertainty of the measurement of $^{86}Kr^+$ is the source of the uncertainty because the calibration was conducted by using the peak position of $^{84}Kr^+$ in the spectrum.

This small difference in the energy can be ascribed to the normal mass shift, δE_{NMS}, given by

$$\delta E_{NMS}=E_{SO}m_e\left(M_{86}^{-1}-M_{84}^{-1}\right), \tag{12}$$

where m_e and M_A are the mass of electron and the mass of nuclei with a mass number of A, respectively [30]. The normal mass shift calculated using Eq. (12) becomes $\delta E_{NMS}=-0.0008$ cm^{-1}, which is consistent with the experimental value of $-0.000\,69(57)$ cm^{-1}.

For ^{83}Kr, having the nuclear spin of $I=9/2$, the peak of $^{83}Kr^+$ exhibits a complex structure originating from the hyperfine splitting. The time evolution of the eigenstate $|J,m_J,I,m_I\rangle$ at $t=0$ is expressed as

$$\begin{aligned}|\phi_{J,mJ,I,mI}(t)\rangle&=\exp\left(-\frac{i\mathcal{H}t}{\hbar}\right)|J,m_J,I,m_I\rangle\\&=\sum_{F,m_F}\exp\left(-\frac{iE_{J,F}t}{\hbar}\right)|J,F,m_F\rangle\\&\quad\times\langle J,F,m_F|J,m_J,I,m_I\rangle.\end{aligned} \tag{13}$$

Because the interaction between the nuclear spin and the laser field is considered to be so small that the magnetic quantum number of the nuclear spin is not changed by the interaction, the time-dependent reduced density matrix

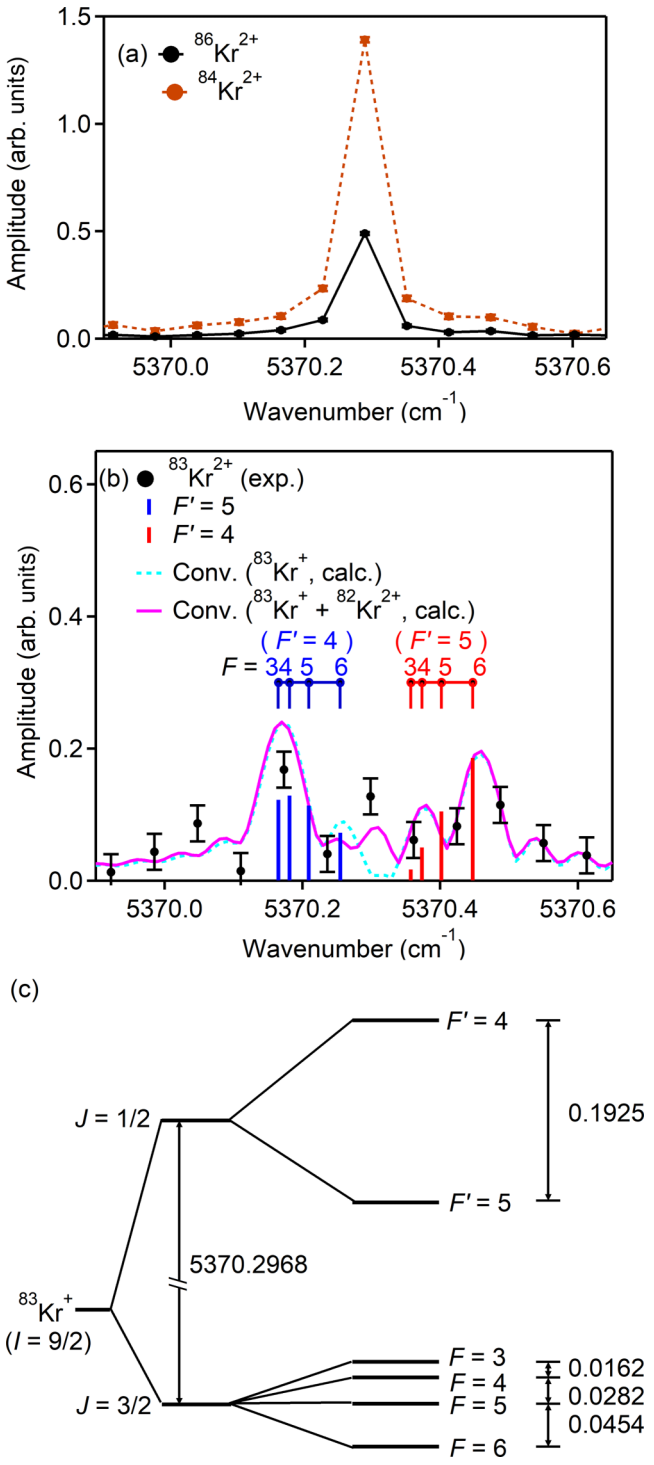

FIG. 5. (a) Fourier transform of the ion yields of $^{86}Kr^{2+}$ (black curve) and $^{84}Kr^{2+}$ (red broken curve) for a comparison. (b) Fourier transform of the ion yields of $^{83}Kr^{2+}$. Black circles: The experimental results. Blue and red sticks: the line strengths of the hyperfine components, $(J = 1/2, F' = 5)$–$(J = 3/2, F)$ and $(J = 1/2, F' = 4)$–$(J = 3/2, F)$, calculated by using Eq. (16). Blue broken curve: theoretically obtained spectrum of $^{83}Kr^{2+}$, which is a convolution of the theoretical line strengths and a sinc function. Purple curve: theoretical spectrum including the effect of the ringing signal of $^{82}Kr^{2+}$. (c) The hyperfine structure of $^{83}Kr^{+}$. The hyperfine splitting energies of $J = 3/2$ and $J = 1/2$ were taken from Refs. [9] and [12], respectively.

elements, $\rho^{m_F,m_F'}_{J,F,J',F'}(t)$, can be expressed as

$$\rho^{m_F,m'_F}_{J,F,J',F'}(t) = \frac{1}{2I+1}\exp\left(\frac{i(E_{J',F'}-E_{J,F})t}{\hbar}\right) \times \sum_{m_I,m_J,m'_J} \rho^{m_J,m'_J}_{J,J'}\langle J,F,m_F|J,m_J,m_I\rangle \times \langle J',m'_J,m_I|J',F',m'_F\rangle, \tag{14}$$

and the time-dependent ionization rate can be described as

$$\Gamma^+(t) = \sum_{J,J',m_J,m'_J,m_I} \langle J,m_J,I,m_I|\hat{\Gamma}^+|J',m'_J,I,m_I\rangle \rho^{m_J,m'_J}_{J,J',m_I}(t). \tag{15}$$

The oscillatory component of Eq. (15) can be described as

$$\Gamma^+_{AC}(t) = \frac{2\sqrt{2}}{3(2I+1)}(\Gamma^+_{1,1,1/2,1/2} - \Gamma^+_{1,0,1/2,1/2}) \times \sum_{m_I,F,F'} \mathrm{Re}\left(\rho^{1/2,1/2}_{3/2,1/2}\exp\left(\frac{i(E_{1/2,F'}-E_{3/2,F})t}{\hbar}\right)\right) \times \left(\left\langle \frac{3}{2_J}, F, \left(m_I+\frac{1}{2}\right)_{m_F}\middle|\frac{3}{2_J},\frac{1}{2_{m_J}},I,m_I\right\rangle \times \left\langle \frac{1}{2_J},\frac{1}{2_{m_J}},I,m_I\middle|\frac{1}{2_J},F',\left(m_I+\frac{1}{2}\right)_{m_F}\right\rangle - \left\langle \frac{3}{2_J},F,\left(m_I+\frac{1}{2}\right)_{m_F}\middle|\frac{3}{2_J},-\frac{1}{2_{m_J}},I,m_I+1\right\rangle \times \left\langle \frac{1}{2_J},-\frac{1}{2_{m_J}},I,m_I+1\middle|\frac{1}{2_J},F',\left(m_I+\frac{1}{2}\right)_{m_F}\right\rangle\right)^2. \tag{16}$$

The line strengths of the hyperfine components were calculated by using Eq. (16) as shown in Fig. 5(b). The line positions of the hyperfine components are obtained from the energy diagram shown in Fig. 5(c). The hyperfine splitting energies were those reported in Refs. [9,12] and the spin-orbit splitting energy of $^{83}Kr^{+}$ was estimated to be 5370.2968 from that of $^{84}Kr^{+}$ obtained in the present measurement including the normal mass shift of 0.0004 cm^{-1}. The line strengths were scaled based on the intensity of the peak in the FT spectrum of $^{84}Kr^{2+}$ and the natural abundances of ^{83}Kr and ^{84}Kr. The hyperfine line spectrum was convoluted by a sinc function, which is an instrumental function of FT spectrum, and is compared with the experimental spectrum as shown in Fig. 5(b). The peaks appearing at 5370.16 and 5370.43 cm^{-1} in the convoluted spectrum, corresponding to the quantum beats of $(J = 1/2, F' = 5)$–$(J = 3/2, F)$ and $(J = 1/2, F' = 4)$–$(J = 3/2, F)$, respectively, can also be seen in the experimental spectrum.

On the other hand, there is a large discrepancy between the peak position in the calculated spectrum and that in the observed spectrum at 5370.3 cm^{-1}. The strong signal at 5370.3 cm^{-1} in the observed spectrum may be ascribed to a ringing signal of $^{82}Kr^{2+}$. As shown in Fig. 1(b), the signal of $^{84}Kr^{2+}$ $(M/Z = 42)$ has also a ringing structure at M/Z~42.5, whose peak intensity is 10% of the main peak. Therefore, it is probable that the ringing signal of $^{82}Kr^{2+}$ $(M/Z = 41)$

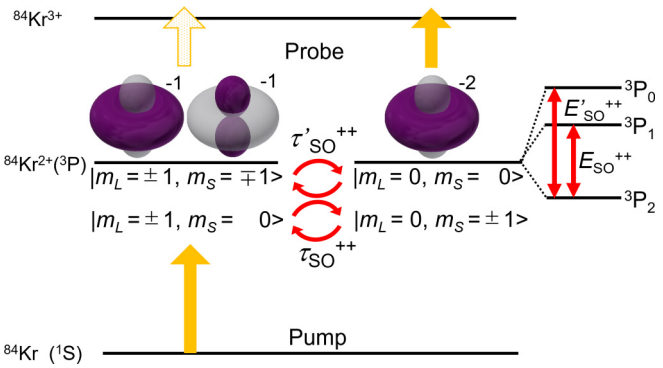

FIG. 6. Energy diagram of Kr^{2+}. The pump pulse creates ^3P ($m_L = \pm 1$) and the populations of ^3P ($m_L = \pm 1$) state and ^3P ($m_L = 0$) state oscillate by spin-orbit interaction with the periods corresponding to E_{SO}^{++} and $E_{SO}^{\prime++}$.

overlaps with the main signal of $^{83}Kr^{2+}$ ($M/Z = 41.5$). The purple curve exhibiting a local maximum at 5370.3 cm^{-1} shows the convoluted spectrum of $^{83}Kr^{2+}$ including 10% of the spectrum of $^{82}Kr^{2+}$, representing the expected ringing signal of $^{82}Kr^{2+}$.

We have examined whether the experimentally obtained spin-orbit splitting energy of $^{84}Kr^+$ is affected by the ringing signal of $^{83}Kr^{2+}$ by subtracting 10% of the calculated spectrum of $^{83}Kr^+$ from the experimental Fourier spectrum of the ion yield of $^{84}Kr^{2+}$, and confirmed that the ringing signal can induce only a negligibly small shift of 5×10^{-5} cm^{-1} in the spin-orbit splitting energy obtained by the least-squares fits, which is one order of magnitude smaller than the uncertainty (5×10^{-4} cm^{-1}).

B. Kr^{2+}

1. The origin of the yield oscillations associated with the electron motion in Kr^{2+}

The ionization of Kr by the pump pulse also creates Kr^{2+} in the lowest electronic ^3P states. Because the tunneling ionization preferentially take place from $m_L = 0$ orbital, the population of Kr^{2+} having the orbital angular momentum of $m_L = \pm 1$ is much larger than that having $m_L = 0$ just after the ionization as shown in Fig. 6. The ^3P ($m_L = \pm 1$) state and the ^3P ($m_L = 0$) state are not a stationary state and must be expressed as a superposition of $^3P_1$ and $^3P_2$ or a superposition of $^3P_0$ and $^3P_2$. Therefore, the population of the ^3P ($m_L = \pm 1$) state prepared by the pump pulse is transferred to the ^3P ($m_L = 0$) state and the population of the ^3P ($m_L = \pm 1$) state and the ^3P ($m_L = 0$) state oscillate with the periods corresponding to the energy separation between $^3P_1$ and $^3P_2$ and the energy separation between $^3P_0$ and $^3P_2$. Because the ionization probability of ^3P ($m_L = \pm 1$) state by the probe pulse is lower than that of the ^3P ($m_L = 0$) state, the ion yields of Kr^{2+} reflects the population of the ^3P ($m_L = \pm 1$) state at the moment of the irradiation by the probe pulse.

In a similar manner as in Sec. III A 2, the motion of an electronic wave packet in Kr^{2+} can be described by using the

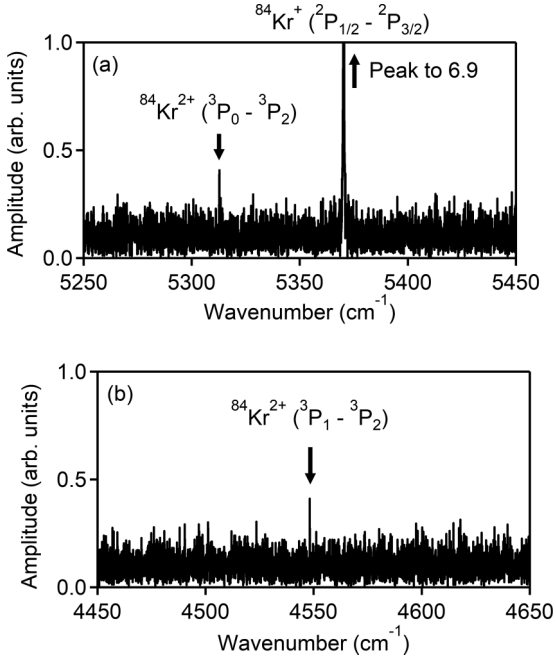

FIG. 7. The sum of the FT spectra obtained by the measurement sets of ^{84}Kr from 5250 to 5450 cm^{-1} (a) and from 4450 to 4650 cm^{-1} (b).

reduced density matrix. The ionization rate of Kr^{2+} to Kr^{3+} can be written as

$$\Gamma^{2+}(t) = \sum_{J,J',m_J,m_J'} \langle \varphi_J^{m_J} | \hat{\Gamma}^{2+} | \varphi_{J'}^{m_J'} \rangle \rho_{J,J'}^{m_J,m_J'}(t), \tag{17}$$

where

$$\hat{\Gamma}^{2+} = \sum_{m_L,m_S} |L, m_L, S, m_S\rangle \Gamma^{2+}_{L,m_L,S,m_S} \langle L, m_L, S, m_S|. \tag{18}$$

By the ionization of Kr to the doubly charged ^3P states, two coherent pairs of the states, $^3P_0^0 - {}^3P_2^0$ and $^3P_1^{\pm 1} - {}^3P_2^{\pm 1}$, are prepared [18]. Therefore, only the matrix elements, $\rho_{0,2}^{0,0}$, $\rho_{2,0}^{0,0}$, $\rho_{1,2}^{\pm 1,\pm 1}$, and $\rho_{2,1}^{\pm 1,\pm 1}$ have nonzero value in the off-diagonal elements in Eq. (17). Equation (17) can be expressed as

$$\begin{aligned}\hat{\Gamma}^{2+}(t) = &\sum_{J,m_J} \langle \varphi_J^{m_J} | \hat{\Gamma}^{2+} | \varphi_J^{m_J} \rangle \rho_{J,J}^{m_J,m_J} \\ &+ \frac{2\sqrt{2}}{3}\left(\Gamma^{2+}_{1,1,1,-1} + \Gamma^{2+}_{1,-1,1,1} - 2\Gamma^{2+}_{1,0,1,0}\right) \\ &\times \mathrm{Re}\left(\rho_{2,0}^{0,0} \exp\left(\frac{i(E_0 - E_2)t}{\hbar}\right)\right) \\ &+ 2\left(\Gamma^{2+}_{1,0,1,1} - \Gamma^{2+}_{1,1,1,0}\right)\mathrm{Re}\left(\rho_{2,1}^{1,1} \exp\left(\frac{i(E_1 - E_2)t}{\hbar}\right)\right).\end{aligned} \tag{19}$$

Similar to the case of the singly charged atom, $\Gamma^{2+}_{1,0,1,0} \gg \Gamma^{2+}_{1,1,1,-1}$ and $\Gamma^{2+}_{1,0,1,1} \gg \Gamma^{2+}_{1,1,1,0}$. Therefore, the ionization rate of Kr^{2+} oscillates with the periods of $\frac{h}{E_{1/2} - E_{3/2}}$ and $\frac{h}{E_{1/2} - E_{3/2}}$, leading to the oscillation of the yield of Kr^{3+} by the probe pulse.

TABLE II. Comparison of the E_{SO} value of Ar^+, Kr^+, and Kr^{2+} (cm^{-1}).

	Ar^+	$^{84}Kr^+$	$^{86}Kr^+$	$^{84}Kr^{2+}$	
Level	$^2P_{1/2} - {}^2P_{3/2}$	$^2P_{1/2} - {}^2P_{3/2}$	$^2P_{1/2} - {}^2P_{3/2}$	$^3P_1 - {}^3P_2$	$^3P_0 - {}^3P_2$
This work	1431.583 33(12)	5370.296 42(50)	5370.295 73(76)	4548.2144(40)	5312.8059(40)
Previous studies	1431.583 1(7)[a]	5370.270(25)[b]	5370.272(25)[b]	4548.4[c]	5312.9[c]
		5370.10[c]	5370.10[c]		

[a]Reference [5].

[b]Obtained from the ionization energy of Kr to $Kr^+(^2P_{3/2})$ [10] and that to $Kr^+(^2P_{1/2})$ [12]. The uncertainty was estimated by $\sigma = \sqrt{\sigma_{3/2}^2 + \sigma_{1/2}^2}$, where σ_J is the uncertainty of the ionization energy to $Kr^+(^2P_J)$.

[c]Reference [3].

2. *Determination of the spin-orbit splitting of* Kr^{2+}

Figure 7 shows the FT spectrum obtained by the summation of all the 14 FT spectra used for the determination of the spin-orbit splitting energies of Kr^+ shown in Fig. 4(b). The peaks corresponding to the energy separations of $^3P_0 - {}^3P_2$ and $^3P_1 - {}^3P_2$ can be seen at ~5312 cm^{-1} and 4548 cm^{-1}, respectively, with the strong peak of the separation of $^2P_{1/2} - {}^2P_{3/2}$ of Kr^+ at ~5370 cm^{-1}. The spectrum was calibrated by using the peak of Kr^+ at 5370.296 42(50) cm^{-1} determined above. The peaks of Kr^{2+} were fitted by a sinc function and the spin-orbit splitting energies were determined to be $E'_{SO}(Kr^{2+}) = 5312.8059(40)\,cm^{-1}$ for $^3P_0 - {}^3P_2$ and $E'_{SO}(Kr^{2+}) = 4548.2144(40)\,cm^{-1}$ for $^3P_1 - {}^3P_2$. The uncertainties include the statistical uncertainty and the systematic uncertainties as summarized in Table I. In the case of Ar, the spin-orbit splitting of Ar^{2+} was not observed. This is because the ionization probability of Ar^{2+} to Ar^{3+} by the probe pulse is low.

C. Comparison with the previous values

The spin-orbit splitting energies obtained by the present study are compared with the literature values in Table II. In our present measurements, the uncertainties associated with the spin-orbit splitting energies of Ar^+, $^{84}Kr^+$, and $^{86}Kr^+$ are of the order of 10^{-4} cm^{-1} and the uncertainties have been reduced by a factor of 6 for Ar^+, a factor of 50 for $^{84}Kr^+$, and a factor of 33 for $^{86}Kr^+$. For $^{84}Kr^{2+}$, the uncertainties in the spin-orbit splitting energies are of the order of 10^{-3} cm^{-1}, which is two orders of magnitude smaller than those of the previously reported values.

IV. SUMMARY

We conducted a strong-field ultrahigh-resolution Fourier transform spectroscopy of Ar^+, Kr^+, and Kr^{2+}. For Ar^+, $^{84}Kr^+$, and $^{86}Kr^+$, the spin-orbit splitting energies have been determined with the relative uncertainties of 1×10^{-7}. The uncertainties have been reduced by a factor of 6 for Ar^+ and by a factor of 50 and 33 respectively for $^{84}Kr^+$ and $^{86}Kr^+$ relative to previous determinations.

By comparing the spin-orbit splitting energies of $^{84}Kr^+$ and $^{86}Kr^+$, we found that the spin-orbit splitting energy of $^{84}Kr^+$ is 0.000 69(57) cm^{-1} larger than that of $^{86}Kr^+$ and this isotope shift is consistent with the normal mass shift. In the case of $^{83}Kr^+$, the peak exhibits complex structure originating from the hyperfine splitting of $^{83}Kr^+$ and the split peak structure was reproduced well by the calculation in which the electronic wave packet represented by $\rho_{J,J}^{m_J,m_J}$ created by the strong-field ionization is assumed to be the same as that of $^{84}Kr^+$.

The spin-orbit splitting of Kr^{2+} also appears in the FT spectrum and the energy interval of $^3P_1 - {}^3P_2$ and that of $^3P_0 - {}^3P_2$ are determined with the relative uncertainty of 1×10^{-6}. The present results have revealed that the energy intervals of atomic ions can be determined with ultrahigh precision by SURF spectroscopy using few-cycle intense laser pulses.

ACKNOWLEDGMENT

The present research was supported by JSPS KAKENHI Grants No. JP15H05696, No. JP19K15500, and No. JP20H00371.

APPENDIX A: LEAST-SQUARE FITTING OF THE PEAKS IN FT SPECTRA

When the amplitude of the oscillation component in the pump-probe signal is constant, a peak in the Fourier transform of the pump-probe signal can be fitted with a sinc function, which is a Fourier transform of a rectangular function. However, in the pump-probe measurement of Ar and D_2, the amplitude of the oscillation component monotonically increases as the time delay increases. The oscillation amplitude at 400 ps $< \Delta t <$ 500 ps is 20% larger than that at 1 ps $< \Delta t <$ 100 ps in the case of Ar^{2+} and 10% larger in the case of $D_2{}^+$. The increase in the amplitude can be ascribed to the time-delay dependent pulse duration of the probe pulse. As the time delay increases, the propagation distance in air of the probe pulse increases, and the pulse duration can be changed by ~0.5 fs by the dispersion of the air [31]. As a result, the peak intensity of the probe pulse varies.

In order to fit the peaks of the FT spectra, we derived a fitting function. When the oscillation component in time domain has a slowly varying envelope, $G(t)$, the fitting function $F(\omega)$ can be obtained by the Fourier transform of a single-frequency component, $A\exp(i\omega_0 t + \theta)$, with the envelope function,

$$F(\omega) = \int A\exp(i\omega_0 t + \theta) G(t) e^{-i\omega t} dt. \quad \text{(A1)}$$

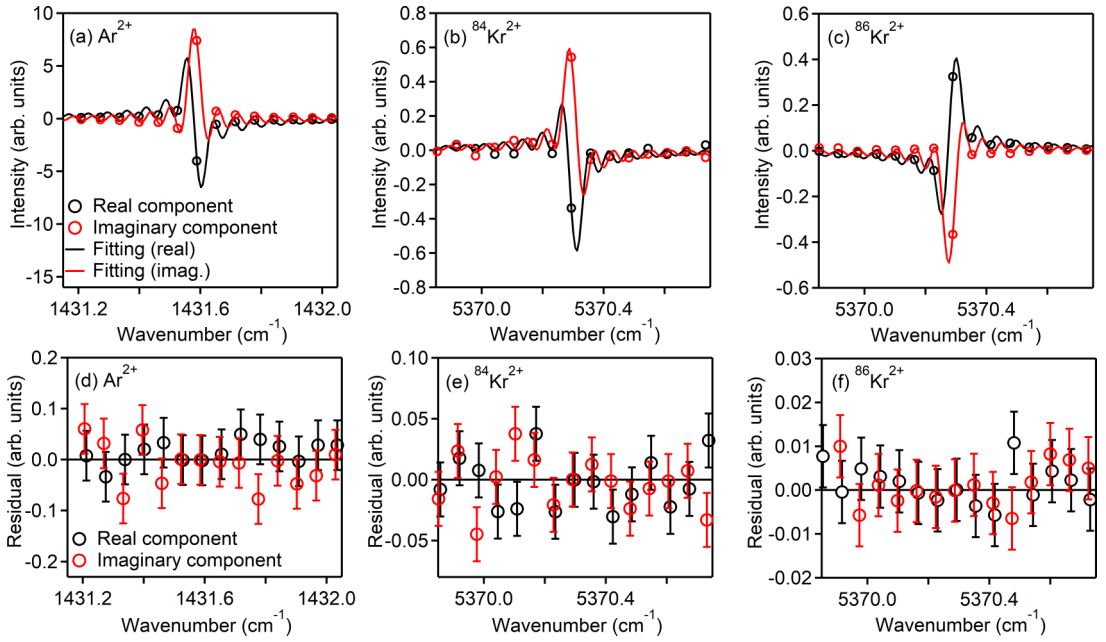

FIG. 8. Best-fit curves obtained by the least-squares fit to the peaks assigned to the spin-orbit splitting in the Fourier transform of the ion yields of (a) Ar^{2+}, (b) $^{84}Kr^{2+}$, and (c) $^{86}Kr^{2+}$. The residuals of the least-squares fits of the peak profiles of (d) Ar^{2+}, (e) $^{84}Kr^{2+}$, and (f) $^{86}Kr^{2+}$. The black and red circles in (a)–(c) represent the real and imaginary components of the FT spectra, respectively. The black and red curves represent the real and imaginary components of the fitting function given by Eq. (A3). The black and red circles in (d)–(f) represent the real and imaginary components of the residuals of the least-squares fits with their uncertainties (σ).

We adopted a truncated Gaussian function as the envelope function,

$$G(\omega) = \begin{cases} \exp\left(-\left(\frac{t-t_0 T}{\alpha T}\right)^2\right) & (0 \leqslant t \leqslant T) \\ 0 & \text{otherwise} \end{cases}, \tag{A2}$$

where T is a stroke of the pump-probe delay (∼500 ps). Equation (A1) leads to

$$F(\omega) = \frac{A\alpha\sqrt{\pi}}{2} e^{i\theta}\left[\exp\left(-\left(\frac{t_0}{\alpha}\right)^2\right)\mathrm{erfcw}\left(\pi\alpha\frac{\omega-\omega_0}{\Delta\omega} + \frac{t_0}{\alpha}i\right) - \exp\left(-\left(\frac{t_0-1}{\alpha}\right)^2 - 2\pi i\frac{\omega-\omega_0}{\Delta\omega}\right)\right.$$
$$\left.\times\ \mathrm{erfcw}\left(\pi\alpha\frac{\omega-\omega_0}{\Delta\omega} - \frac{t_0-1}{\alpha}i\right)\right], \tag{A3}$$

where $\Delta\omega = 2\pi/T$ is a resolution of the Fourier spectrum and erfcw(z) is a scaled complex complementary error function expressed as Eq. (9). Examples of the least-squares fits of the peaks in the FT spectra and the residual of the least-squares fits are shown in Fig. 8. The uncertainty in the peak energy and the uncertainty in the residuals were estimated from the root-mean-square of the spectral intensities in the frequency ranges in which there are no peaks.

APPENDIX B: ZEEMAN EFFECT

Under the magnetic field, the time evolution of the rare-gas atom cations can be written as

$$|J, m_J\rangle_t = \exp\left(-\frac{i\mathcal{H}t}{\hbar}\right)|J, m_J\rangle$$
$$= \sum_{m''_J, m'_J} |J, m''_J\rangle d^J_{m''_J, m'_J}(-\phi)\exp\left(-\frac{iE_{J,m'_J}t}{\hbar}\right)d^J_{m'_J, m_J}(\phi)$$
$$E_{J,m'_J} = E_J + \mu_B g_J B m'_J, \tag{B1}$$

where $d^J_{m'_J, m_J}(\phi)$ is an element of Wigner d matrices, ϕ is the angle between the laser polarization direction and the direction of the geomagnetic field, and g_J is the Landé g factor. By adopting Eqs. (B1) to (4), the time-dependent component at ∼5370 cm^{-1},

$\hat{\Gamma}^{+}_{\mathrm{AC}}$, is written as

$$\hat{\Gamma}^{+}_{\mathrm{AC}} = \frac{2\sqrt{2}}{3}(\Gamma_{1,1} - \Gamma_{1,0}) \sum_{mJ,\ mJ'} \left(d^{3/2}_{m'_J,1/2}(\phi) d^{1/2}_{m_J,1/2}(\phi) - d^{3/2}_{m'_J,-1/2}(\phi) d^{1/2}_{m_J,-1/2}(\phi)\right)^2 \mathrm{Re}\left(\exp\left(-\frac{i\left(E_{1/2,m_J} - E_{3/2,m'_J}\right)t}{\hbar}\right)\rho^{1/2,1/2}_{3/2,1/2}\right). \tag{B2}$$

According to Eq. (B2), the Zeeman components $(J, m_J) - (J', m'_J)$ and $(J, -m_J) - (J', -m'_J)$ have the same peak amplitudes. Therefore, the center of the gravity of the Zeeman components is $E_{1/2} - E_{3/2}$, which is the same as the spin-orbit splitting energy.

[1] W. Persson, Phys. Scr. **3**, 133 (1971).
[2] S. Bakin and J. O. Stoner, Jr., *Atomic Energy Level and Grotrian Diagrams* (Elsevier Science Ltd., New York, 1978), Vol. 2.
[3] E. B. Saloman, J. Phys. Chem. Ref. Data **36**, 215 (2007).
[4] J. E. Hansen and W. Persson, Phys. Scr. **36**, 602 (1987).
[5] C. Yamada, H. Kanamori, and E. Hirota, J. Chem. Phys. **83**, 552 (1985).
[6] F. Brandi, I. Velchev, W. Hogervorst, and W. Ubachs, Phys. Rev. A **64**, 032505 (2001).
[7] H. J. Wörner, M. Grütter, E. Vliegen, and F. Merkt, Phys. Rev. A **71**, 052504 (2005).
[8] M. Schäfer, M. Raunhardt, and F. Merkt, Phys. Rev. A **81**, 032514 (2010).
[9] H. J. Wörner, U. Hollenstein, and F. Merkt, Phys. Rev. A **68**, 032510 (2003).
[10] U. Hollenstein, R. Seiler, and F. Merkt, J. Phys. B: At. Mol. Opt. Phys. **36**, 893 (2003).
[11] M. Schäfer and F. Merkt, Phys. Rev. A **74**, 062506 (2006).
[12] T. A. Paul, J. Liu, and F. Merkt, Phys. Rev. A **79**, 022505 (2009).
[13] A. Fleischer, H. J. Wörner, L. Arissian, L. R. Liu, M. Meckel, A. Rippert, R. Dörner, D. M. Villeneuve, P. B. Corkum, and A. Staudte, Phys. Rev. Lett. **107**, 113003 (2011).
[14] L. Fechner, N. Camus, J. Ullrich, T. Pfeifer, and R. Moshammer, Phys. Rev. Lett. **112**, 213001 (2014).
[15] E. Goulielmakis, Z.-H. Loh, A. Wirth, R. Santra, N. Rohringer, V. S. Yakovlev, S. Zherebtsov, T. Pfeifer, A. M. Azzeer, M. F. Kling, S. R. Leone, and F. Krausz, Nature (London) **466**, 739 (2010).
[16] A. Wirth, R. Santra, and E. Goulielmakis, Chem. Phys. **414**, 149 (2013).
[17] Z.-H. Loh and S. R. Leone, J. Phys. Chem. Lett. **4**, 292 (2013).
[18] Y. Kobayashi, M. Reduzzi, K. F. Chang, H. Timmers, D. M. Neumark, and S. R. Leone, Phys. Rev. Lett. **120**, 233201 (2018).
[19] M. Kübel, Z. Dube, A. Y. Naumov, D. M. Villeneuve, P. B. Corkum, and A. Staudte, Nat. Commun. **10**, 1042 (2019).
[20] T. Ando, A. Shimamoto, S. Miura, A. Iwasaki, K. Nakai, and K. Yamanouchi, Commun. Chem. **1**, 7 (2018).
[21] T. Ando, A. Iwasaki, and K. Yamanouchi, Mol. Phys. **117**, 1732 (2019).
[22] T. Ando, A. Iwasaki, and K. Yamanouchi, Phys. Rev. Lett. **120**, 263002 (2018).
[23] J. Emsley, *The Elements, Oxford Chemistry Guides* (Oxford University Press, New York, 1995).
[24] T. Ergler, B. Feuerstein, A. Rudenko, K. Zrost, C. D. Schröter, R. Moshammer, and J. Ullrich, Phys. Rev. Lett. **97**, 103004 (2006).
[25] A. M. Perelomov, V. S. Popov, and M. V. Terent'ev, Sov. Phys. JETP **23**, 924 (1966).
[26] M. V. Ammosov, N. B. Delone, and V. P. Krainov, Sov. Phys. JETP **64**, 1191 (1986).
[27] N. Rohringer and R. Santra, Phys. Rev. A **79**, 053402 (2009).
[28] H. J. Wörner and P. B. Corkum, J. Phys. B: At. Mol. Opt. Phys. **44**, 041001 (2011).
[29] M. L. Niu, E. J. Salumbides, G. D. Dickenson, K. S. E. Eikema, and W. Ubachs, J. Mol. Spectrosc. **300**, 44 (2014).
[30] H. A. Schuessler, A. Alousi, R. M. Evans, M. Brieger, F. Buchinger, and Y. F. Li, Phys. Rev. Lett. **65**, 1332 (1990).
[31] P. E. Ciddor, Appl. Opt. **35**, 1566 (1996).